Seismic response to evolving injection at the Rotokawa geothermal field, New Zealand

Chet Hopp[a,b], Steven Sewell[a], Stefan Mroczek[a,c], Martha Savage[a], John Townend[a]

[a] *School of Geography, Environment and Earth Sciences, Victoria University of Wellington, PO Box 600, Wellington, NZ, 6140*
[b] *Now at: Lawrence Berkeley National Laboratory, Energy Geosciences Division, 1 Cyclotron Rd, Berkeley, CA 94720*
[c] *Now at: GFZ German Research Centre for Geosciences, Potsdam, Germany and Freie University Berlin, Germany*

Abstract

Catalogs of microseismicity are routinely compiled at geothermal reservoirs and provide valuable insights into reservoir structure and fluid movement. Hypocentral locations are typically used to infer the orientations of structures and constrain the extent of the permeable reservoir. However, frequency-magnitude distributions may contain additional, and underused, information about the distribution of pressure. Here, we present a four-year catalog of seismicity for the Rotokawa geothermal field in the central Taupō Volcanic Zone, New Zealand starting two years after the commissioning of the 140 MWe Nga Awa Purua power station. Using waveform-correlation-based signal detection we double the size of the previous earthquake catalog, refine the location and orientation of two reservoir faults and identify a new structure. We find the rate of seismicity to be insensitive to major changes in injection strategy during the study period, including the injectivity decline and shift of injection away from the dominant injector, RK24. We also map the spatial distribution of the earthquake frequency-magnitude distribution, or b-value, and show that it increases from $\sim$1.0 to $\sim$1.5 with increasing depth below the reservoir. As has been proposed at other reservoirs, we infer that these spatial variations reflect the distribution of pressure in the reservoir, where areas of high b-value correspond to areas of high pore-fluid pressure and a broad distribution of activated fractures. This analysis is not routinely conducted by geothermal operators but shows promise for using earthquake b-value as an additional tool for reservoir monitoring and management.

Keywords: Induced seismicity, fluid injection, b-value, geothermal, New Zealand

1. Introduction

Geothermal operators routinely monitor the rates and locations of microseismic activity at developed reservoirs. Typically, the location of seismicity is assumed to correlate with regions where pore-fluid pressure has been artificially elevated by fluid injection (e.g. Sherburn et al., 2015; Garcia et al., 2016, but see Riffault et al., 2018). In turn, these areas are assumed to correspond to major flow pathways in the reservoir, which are of paramount importance in understanding reservoir dynamics and planning injection/extraction well targets. In addition, reservoir structures can be accurately imaged from high-precision earthquake hypocentral locations, as can the extent of the permeable reservoir (e.g. Garcia et al., 2016; Kwiatek et al., 2014; Martínez-Garzón et al., 2014).

However, much of the information contained in even a basic earthquake catalog can go unused by reservoir managers. In particular, while earthquake magnitudes are often used to characterize the risk of large-magnitude induced seismicity, this information goes relatively unused from the standpoint of reservoir characterization. In a limited number of cases, the relative abundance of small- and large-magnitude events (usually described by the parameter b), has been used to infer reservoir properties such as pore-fluid pressure and the extent of fracturing. For example, Bachmann et al. (2012) modeled b-value and pore-fluid pressure for the case of the Basel enhanced geothermal injection well, showing that, from a theoretical standpoint, b is expected to decrease exponentially with distance from a given injection point, but that b actually increased between the wellbore and 200 m.

In this paper we focus on the Rotokawa geothermal field in the central Taupō Volcanic Zone (TVZ) of New Zealand. The field was initially developed in 1997 but has since undergone large-scale development, most notably the commissioning of the 140 MWe Nga Awa Purua (NAP) plant in 2010 (McNamara et al., 2016). The seismic dataset analyzed here (2012–2015) spans a period of stabilization, during which the reservoir was equilibrating to the increased extraction required by the installation of NAP. We use a matched-filter earthquake detection technique to substantially increase the number of events in our catalog relative to standard, automatic detection. We then calculate magnitudes for the newly-detected events, again using a waveform correlation-based technique, before precisely relocating each event.

The Rotokawa reservoir has been extensively studied over its two decades of development. The current understanding of the reservoir is based on research by a number of groups who have identified at least four compartments, which are likely bounded by several faults acting as barriers to inter-compartment fluid flow (Sewell et al., 2015a; Addison et al., 2017; Wallis et al., 2013). Previous studies of microseismicity at Rotokawa have been used to constrain the location of one of these structures, the Central Field Fault (CFF), but as seismicity only occurs in the injection field, these studies have not revealed structures in other parts of the reservoir (Sherburn et al., 2015; Sewell et al., 2015b).

In the following analyses, we compare our catalog to those of previous studies of microseismicity at Rotokawa (Sewell et al., 2015b; Sherburn et al., 2015)

and relate the rate and location of seismicity to changes in injection strategy. We also map the frequency-magnitude distribution (b-value) within the field, something which has not been done at Rotokawa before. When combined with high-precision locations, the complex patterns in b-value show potential for mapping pore-pressure and/or fracturing extent at reservoir scale.

1.1. Rotokawa resource development

As with most of the TVZ geothermal fields, the existence of the Rotokawa resource was originally verified through a New Zealand government-funded drilling program starting in the 1960's (Cole and Legmann, 1998). The first resource consent was granted to the Tauhara No. 2 Trust and various other entities in 1993. Electricity generation began in 1997 with the installation of the 24 MWe Rotokawa A (RGEN) combined-cycle power plant (Legmann and Sullivan, 2003). In 2000, Mercury NZ Ltd. (then trading as Mighty River Power) combined with the Tauhara No. 2 Trust to form the Rotokawa Joint Venture, which continues to oversee development at Rotokawa (Legmann and Sullivan, 2003).

Prior to 2005, reinjection at Rotokawa took place at depths of <1000 m (Sewell et al., 2015a) but was moved to greater depths (1000–3000 m) due to pressure buildup in the shallow injection zone (McNamara et al., 2016). Additional resource consents were granted to the Rotokawa Joint Venture in 2007, prompting the drilling of 16 additional wells (RK19–RK35) and culminating in the commissioning of the NAP plant in 2010. This brought the total installed capacity at Rotokawa to 174 MWe fed by 60,000–65,000 tons/day of fluid from the reservoir (McNamara et al., 2016). The additional information provided by the new wells allowed for significant improvements to the reservoir conceptual model detailed by Sewell et al. (2015a) and McNamara et al. (2016).

1.2. Rotokawa operations changes

The dataset analyzed in this work spans the four years starting in 2012 and ending at the end of 2015. During this period, little new development was undertaken at Rotokawa as the resource was adjusting to the significant increase in production associated with the commissioning of NAP in 2010. Changes in injection and production are therefore more subtle than those analyzed at the nearby Ngatamariki field for the same period, where more substantial changes were associated with well stimulation and power plant commissioning (Clearwater et al., 2015; Hopp et al., 2019). Table 1 contains periods identified by the operator, Mercury, from 2012–2015 during which the character of seismicity may help address various outstanding questions about the nature of the reservoir.

As is typically the case for produced reservoirs of any type (e.g. natural gas, oil, geothermal), seismicity at Rotokawa is caused predominantly by the injection, not the extraction, of fluids. This is because injection increases pore fluid pressure, thereby destabilizing fracture networks, whereas extraction achieves the opposite, although stress changes induced by the removal of reservoir volume are capable of triggering earthquakes (Segall, 1989; National Academy of

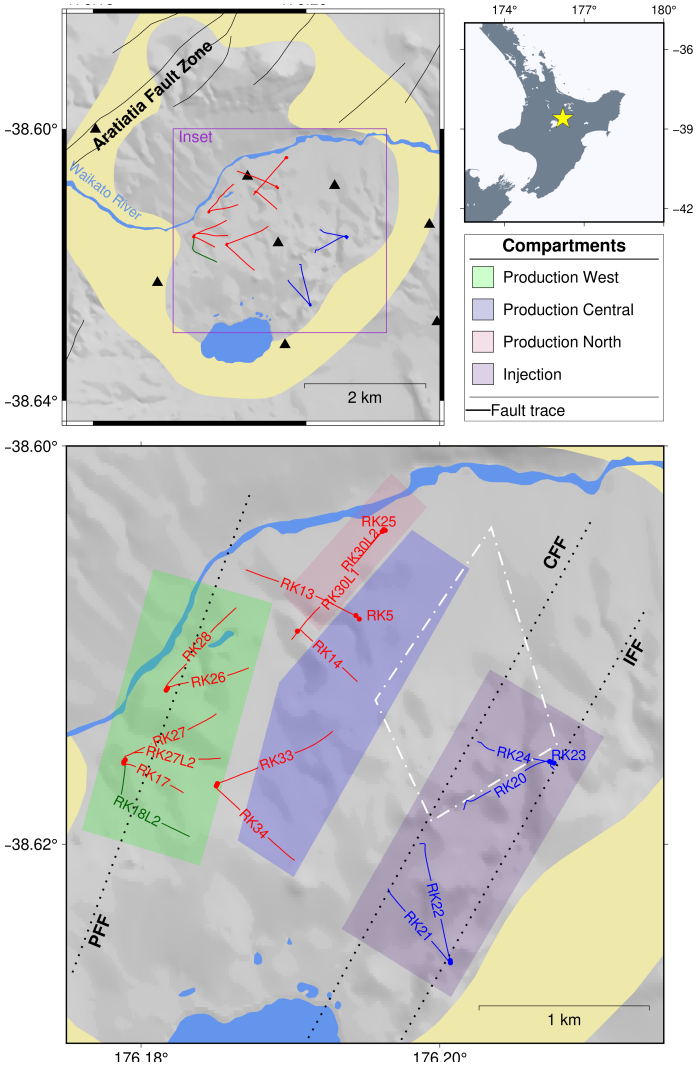

Figure 1: Overview of the Rotokawa geothermal field. The top right panel shows the location of the field on the North Island of New Zealand (yellow star). The top left panel shows the resistivity boundary of the field in yellow and injection and production wells in blue and red, respectively. Solid black lines are active faults. The lower panel shows a closeup of the field, with the well names labeled and the modeled surface traces of the three known faults (PFF, CFF, IFF) shown as black dotted lines. The white dot-dashed line shows the extent of significant seismicity from 2008–2012, as reported by Sherburn et al. (2015). There are four known compartments in the Rotokawa reservoir shown as colored polygons. Each is semi-isolated from the others by either a permeability contrast or impermeable barrier (i.e. a fault). The production field comprises three compartments, the west, central and north (green, blue and red, respectively). The injection field is shaded in purple and is a separate compartment.

Field	Operation	Start	End
Rotokawa	RK24 injectivity decline	2012	2013
Rotokawa	Switch of injection: RK24–RK23	2014-6	2014-7
Rotokawa	RK34 drilling losses	2014-9	2014-11
Rotokawa	Plant shutdowns and startups	2012–2015	2012–2015

Table 1: Periods of interest in 2012–2015

Sciences, 2013). For this reason, the periods defined by Mercury correspond predominantly to changes in injection operations. The first two periods listed in Table 1 correspond to a period of injectivity decline in the dominant injection well RK24 (Figure 1) due to an unknown cause. In response to the well's declining ability to accept injectate from the power plants, excess fluid was shifted to well RK23 (Figure 1).

From September to November 2014, Mercury drilled an additional production well, RK34. At reservoir depths, the drilling operation sustained full fluid losses. Similar drilling losses induced a large number of seismic events during drilling in southern Ngatamariki (Hopp et al., 2019) and may have had a similar effect at Rotokawa. Finally, swarm-like behavior (defined as any day on which more than 15 events occurred) has been observed at Rotokawa in the past and is thought to be related to pressure perturbations induced by power plant shutdown and startup during regular maintenance operations (Sewell et al., 2015b).

The fluid injected at Rotokawa varies by application and between individual wells. For instance, during the drilling of RK34, the drilling fluid was composed predominantly of water at an ambient temperature of 10–20°C. During standard plant operations, the injectate at each injection well is either condensate (the product of cooling the steam used to turn the turbines), concentrated brine (brine from which condensate has been removed), or some combination of these end members. During most of the study period, brine and condensate from NAP were injected into RK23-24, while fluid from RGEN was injected into RK20. Depending on the mixture, fluid entered the injection wells at a temperature of between $\sim$ 40°C and 130°C.

1.3. Reservoir model

The hydrogeological behavior of the Rotokawa reservoir is strongly influenced by three regional NE–SW-striking faults, each named for its location relative to the injection or production field. From east to west they are: the Injection Field Fault (IFF), Central Field Fault and Production Field Fault (PFF) (Wallis et al., 2013, Figure 1). The existence and orientation of these faults are known from well cuttings that show vertical offsets in the top of the Rotokawa Andesite (and other units) between wells. The CFF, for instance, is interpreted to have a throw of nearly 400–500 m between the injection and production wells, while the IFF and PFF have accommodated vertical displacements of 250–350 m (Wallis et al., 2013). Several independent datasets have been used to corroborate the presence of these faults, including tracer returns (Addison et al., 2015, 2017),

pressure compartmentalization (Quinao et al., 2013; Sewell et al., 2015a) and previous studies of microseismicity (Sherburn et al., 2015; Sewell et al., 2015b).

Lateral pressure gradients within the Rotokawa reservoir of as much as ∼8 MPa/km indicate that it is made up of several discrete compartments that either have different permeabilities or are separated by structures that act as cross-strike flow barriers (Quinao et al., 2013; Sewell et al., 2015a). The three major faults mentioned above act either as barriers between these compartments or as conduits for fluid flow within compartments. Slow or nonexistent tracer returns from injection to production indicate that the CFF is such a barrier, isolating the injection compartment from each of the production compartments (Figure 1). However, this isolation is not constant along the strike of the CFF (Addison et al., 2017). Current modeling by Mercury suggests that a 'leaky' connection exists between the main injection well, RK24 and the central production wells (RK5, RK14, RK29; blue polygon in Figure 1), which provides pressure support to these production wells. This pressure support is not present in the western (4.2 MPa drawdown) or northern (3 MPa drawdown) production field compartments (green and red, respectively in Figure 1; Quinao et al., 2013; Addison et al., 2017).

Strong pressure connection between the wells within the western production compartment suggests that the PFF acts as an along-strike fluid conduit, transmitting pressure signals quickly to distances of as much as a kilometer (Quinao et al., 2013; Sewell et al., 2015a; McNamara et al., 2016). These pressure observations are well correlated with the geologic offsets observed in the borehole cuttings mentioned above (Wallis et al., 2013).

There is less evidence to indicate what role the IFF plays in reservoir behavior. Some evidence suggests that there is a pressure connection between wells RK20, RK23 and RK24, implying that the three boreholes are located in a single reservoir compartment (Quinao et al., 2013). However, vertical stratigraphic offsets (250–300 m) between RK23 and boreholes RK20 and RK24 indicate that RK23 lies to the east of a significant structure (i.e. the IFF) whereas RK20 and RK24 lie to the west (Wallis et al., 2013). In addition, bottom-hole temperatures in RK20/24 are ∼40°C higher than in RK23, only ∼500 m away, indicating a lateral variation in reservoir properties between the wells (e.g. permeability). In this work we adopt the interpretation of Wallis et al. (2013) that places the IFF between boreholes RK20/RK24 and RK23.

1.4. Previous work

The Taupō Volcanic Zone is a region of backarc extension associated with the westward subduction of the Pacific Plate beneath the North Island of New Zealand (at ∼45 mm/yr; Cole and Lewis, 1981; Wilson et al., 1995; DeMets et al., 1994). Within the overriding Australian Plate, the rate of NW–SE spreading ranges from 15 mm/yr in the north to <5 mm/yr in the south (Wallace, 2004), most of which is accommodated within the Taupō Fault Belt (TFB), which lies just to the NW of Rotokawa (Villamor et al., 2011). This extension constitutes the main driving force for seismicity in the region, most of which

occurs within the TFB at rates and magnitudes similar to or exceeding that of the seismicity within the geothermal fields (Sherburn et al., 2015).

Previous studies of the seismicity at Rotokawa were conducted for the years 2008–2012 by GNS Science and Mercury (Sherburn et al., 2015; Sewell et al., 2015b) and as part of a Master's thesis at Victoria University of Wellington (Rawlinson, 2011). These studies revealed a pattern of seismicity that shifted with time as the injection and production strategies evolved in response to field development and reservoir understanding. As of the end of 2012, Sherburn et al. (2015) identified the currently-active area of seismicity as that bounded by the white, dot-dashed diamond shown in Figure 1. This cluster of seismicity occurred at the approximate depth of the permeable zones in wells RK20, RK23 and RK24, which together accounted for nearly all of the deep injection into the Rotokawa reservoir at the time. This cluster was inferred to be bounded to the northwest by the CFF (Figure 1), corroborating the evidence from tracer testing that fluid flow was impeded across the structure, allowing pressure buildup and reservoir cooling east of the fault and inducing seismicity (Sherburn et al., 2015; Sewell et al., 2015b).

Within the reservoir, Sherburn et al. (2015) and Sewell et al. (2015b) cited the relatively modest wellhead pressures measured in the injection field (<1.5 MPa) as evidence for cooling-dominated, and not pressure-dominated, triggering of seismicity at Rotokawa. However, stress changes as low as 10^{-2} MPa have been shown to trigger seismicity in many settings (Stein, 1999; Keranen and Weingarten, 2018). As Sewell et al. (2015b) noted, the large temperature gradients induced at the injection wells (>180°C) certainly produce stress changes of tens of MPa within 10–100s of meters of the well, especially when large volumes are injected over years (Stephens and Voight, 1982). Though the effect of cooling on fracture stability is complex (Jeanne et al., 2015b), these cooling effects likely do dominate earthquake triggering close to the injection wells. However, the occurrence of seismicity beyond a ∼500 m radius and the lack of measurable cooling at the production wells (including those that receive pressure support from the injection zone) indicates that other effects, including pore-pressure increase and poroelastic stress transfer, also play a role in earthquake triggering at Rotokawa (e.g. Schoenball et al., 2012).

2. Data and methods

2.1. Data

As described in detail by Hopp et al. (2019), the Mercury seismic network covers an area of approximately 450 km^2 surrounding the Rotokawa and Ngatamariki geothermal areas. While most of the instruments are 4.5 Hz Geospace GS-11D short-period geophones owned by Mercury, we have also incorporated a number of stations operated by Contact Energy at their nearby Wairakei geothermal field, as well as three broadband instruments and one short-period instrument operated by the GeoNet national network (Figure S1). At any one time in 2012–2015, as few as 15 and as many as 29 instruments were operational.

GNS Science, under contract to Mercury, provided the initial earthquake catalog used in this study. The raw waveform data were collected quarterly from Mercury's data loggers and supplemented by data from the GeoNet stations. Events were automatically detected and located using the *SeisComP3* software package (Weber et al., 2007). We discarded all events located >5 km outside the bounds of the Rotokawa resistivity boundary (yellow shaded area, Figure 1), so that a total of 2665 microearthquakes of between M_L 0.37 and 3.52 remained. We relocated these events using first the nonlinear location program *NonLinloc* (Lomax et al., 2014) and then the double-difference relocation software *GrowClust* (Trugman and Shearer, 2017) before undertaking the following analyses.

Production and injection well locations, temperatures, flow rate and pressures were provided by Mercury.

2.2. Matched-filter detection

We used the matched-filter correlation detection approach described by Hopp et al. (2019) to increase the number of events included in the GNS Science earthquake catalog mentioned above. This approach increases the number of events detected without unduly increasing the rate of false detection and is well suited to detection at geothermal fields with many noise sources and dense clusters of small seismic events.

From the automatically-detected, GNS Science catalog we took only those events having average pick residuals within one standard deviation of the mean pick residual for the entire catalog. Each of the resulting 2665 events was used as a 'template' event. Each template consists of one-second-long waveforms, starting 0.1 seconds before the P-pick. We chose not to use the horizontal channels after inspection of the GNS automatic S-picks revealed a significant number of mis-picked arrivals. After applying an anti-aliasing filter, both continuous and template waveforms were sampled at 50 Hz and filtered from 3.0 to 20.0 Hz.

To generate detections, templates were cross-correlated with continuous data at a rate of 50 samples per second. At each epoch, the cross-correlation coefficients for each channel of data were summed to create the network detection statistic (Shelly et al., 2007). A detection was recorded whenever the detection statistic exceeded a threshold value, which in this case was defined as the daily median absolute deviation (MAD) of the detection statistic multiplied by eight (as suggested by Shelly et al., 2007; Matson, 2019). Duplicate detection removal was conducted by looping through all detections in order of descending detection statistic and removing detections within a user-defined time buffer of two seconds. We adopted two seconds for the time buffer following a visual review of template events that revealed numerous cases of near-repeating seismicity with inter-event times of 3–5 s.

Visual inspection of a subset of the detection waveforms showed that false detections occurred at a rate of approximately 1–3 false detections per day. However, there are too many detections (>100,000) to inspect them all manually. Therefore, we employ a sequence of thresholds based on the correlation between the template and detected waveforms in order to exclude lower-quality

events, thus suppressing the number of false detections in our final catalog. These thresholds were applied during the location and magnitude calculation procedures described below. We visually inspected thousands of waveforms from the final catalog while manually picking first-motion polarities and encountered no false detections.

2.3. NonLinLoc locations

For each newly-detected event, P-picks were made at each channel included in the template via an automated workflow. For each station, the template and detected waveforms were correlated over a 0.2 second window centered on the detection time. Picks were recorded at the time corresponding to the highest correlation value within that window. If the correlation value of the template and detected waveform fell below 0.4, the pick was discarded. We then discarded those events with five or fewer picks. For the remaining events, we made automatic S-picks using the method developed by Diehl et al. (2009) and modified by Castellazzi et al. (2015), a process detailed by Mroczek et al. (2019). We located the remaining events with the nonlinear location program *NonLinLoc* (Lomax et al., 2014) using a preliminary 1-D model computed with *VELEST* (Kissling et al., 1994; Sewell et al., 2017, Table S2).

2.4. Magnitudes

We calculated magnitudes for each of the newly-detected events using an approach originally developed by Shelly et al. (2016). The specific approach used here was described in detail by Hopp et al. (2019) and relies on the assumption that the relative amplitude between a template event (for which a magnitude had been calculated by GNS Science) and the detected event represents their relative moment. This relative moment can then be used to calculate the magnitude of the detected event.

We calculated relative amplitudes only when the cross-correlation coefficient between the template and detection exceeded 0.6 at any given station. For event pairs with a minimum of four common stations exceeding the correlation threshold, we calculated the relative moment as the median of the relative amplitudes, following Shelly et al. (2016). This procedure left 25,148 events with calculated magnitudes. As the relative amplitudes are calculated from waveforms recorded at the same station, there is no need to remove the instrument response.

We used the local magnitude (M_L) of each template to calibrate the relative moment calculations from the method above and produce M_L estimates for each detection. This was done by first converting the template M_L to moment magnitude (M_w) using the scaling relationship

$$M_L = 0.97M_w + 0.14 \tag{1}$$

determined for locally detected, shallow New Zealand earthquakes (Ristau et al., 2016) and then converting to seismic moment using the well-known relation

(Hanks and Kanamori, 1979)

$$M_w = \frac{2}{3} \log_{10} M_0 - 9 \tag{2}$$

Knowing the relative moment of the template event from the procedure outlined above, we then determined the relationship between the relative moments and actual moment, which allowed us to convert relative moments to M_w and then back to M_L using Equation 1. After applying this methodology, 28,414 events remained in our catalog.

2.5. GrowClust locations

The catalog was relocated using the double-difference relocation program *GrowClust* (Trugman and Shearer, 2017) using the same 1D velocity model used in the *NonLinLoc* relocation above. A detailed comparison of the *NonLinLoc* and *GrowClust* locations can be found in Hopp (2019). Differential travel times were generated using the Python package *hypoDDpy* (Krischer, 2015) with a 1 s correlation window, a maximum time shift of 0.2 s and a minimum cross-correlation value of 0.6. Here we chose a longer correlation window of 1 s than for the arrival time picking detailed in Section 2.3 and a higher correlation threshold (the same as used for the magnitude calculation above) to ensure only the best-correlated subset of picks were used for differential time calculations. These picks were visually verified using the obspy function, xcorr_pick_correction (Team, 2019). We were able to relocate nearly 6500 events using this method. Further details were provided by Hopp (2019), including comparisons of the two location methods.

2.6. b-value calculation

The frequency-magnitude relationship for earthquake catalogs is a power-law distribution described by Gutenberg and Richter (1942) as

$$\log N = a - bM \tag{3}$$

where a increases with the number of earthquakes in the catalog, b describes the distribution of earthquake magnitudes above the catalog magnitude of completeness (M_c) and N is the number of events larger than magnitude M. We calculate M_c for the catalogs presented here following the methodology of Wiemer (2000). For a range of M_c values, a and b are determined for our earthquake catalog and an idealized synthetic distribution is constructed with the same a and b values. The absolute difference between the synthetic and measured distributions given by Wiemer (2000) is:

$$R(a, b, M_i) = 100 - \left(\frac{\sum_{M_i}^{M_{max}} |B_i - S_i|}{\sum_i B_i} 100 \right) \tag{4}$$

where M_{max} is the maximum observed magnitude and B_i and S_i are the observed and predicted number of events in a given magnitude bin, i. This residual is then minimized to find the most appropriate M_c (Figure 2).

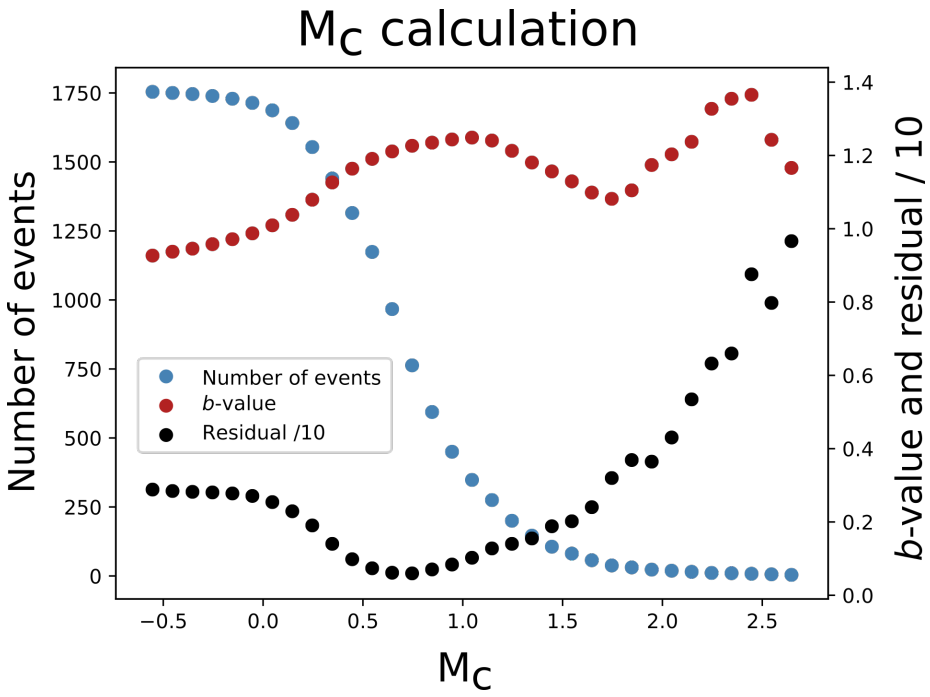

Figure 2: Illustration of the magnitude of completeness calculation developed by Wiemer (2000). Black dots indicate the normalized, absolute difference between the observed and theoretical distribution of events for a given M_c and *b*-value (shown here divided by 10 to better fit the plot). Blue dots show the total number of events used for the fit at each magnitude of completeness and red dots show the corresponding *b*-value.

We map *b*-value spatially using the approach described by Bachmann et al. (2012), whereby, for each event in the *GrowClust*-relocated catalog (which they refer to as a 'focus'), the nearest n events are selected and M_c is calculated for this subset, which we call a "sub-catalog". During initial testing of this procedure, b and M_c exhibited colinear behavior, implying that we were introducing a bias wherein a spatially varying M_c led to a varying *b*-value. To eliminate this bias, we compare the M_c of each sub-catalog with that of the catalog as a whole (0.74). If the sub-catalog M_c is greater than that of the entire catalog, we discard it. If the sub-catalog M_c is less than that of the entire catalog, we then enforce an M_c of 0.74. If the number of events larger than M_c=0.74 exceeds a threshold, the *b*-value is calculated and mapped to the focus event's location using the maximum-likelihood method such that (Aki, 1965; Shi and Bolt, 1982).

$$b = \log e \frac{1}{\bar{M} - M_c} \tag{5}$$

where $\bar{M}$ is the mean magnitude of the events larger than the magnitude of completeness, M_c. Bachmann et al. (2012) map the *b*-value for the 150 nearest

events, with a threshold of 25 events greater than M_c. Here we use the nearest 300 events with a minimum threshold of 100 events above M_c.

This method introduces a potential bias due to the fact that each of the focus-centered subcatalogs will occupy a different volume of the crust than the last. As a larger volume of crust is considered, the probability of intersecting a feature that might disrupt the fractal scaling of fracture sizes (e.g. a structure longer than the maximum dimension of the volume of the catalog or a geologic contact) increases, possibly skewing the b-value (Langenbruch and Shapiro, 2014). For the case of Rotokawa, as shown in Figure S2, there is a weak negative correlation between b-value and the volume occupied by the catalog. Those sub-catalogs with the mean volume of $\sim 1.72 \times 10^8$ m^3 (i.e. a sphere with a radius of $\sim$500 m) have a wide range of b-values ($\sim$0.8–1.5), indicating that b-value variation is likely controlled by factors other than catalog volume.

One possible, yet poorly understood, complication in calculating b-values for our catalog arises from the use of the matched-filter detection routine. A template event can only detect events with the same (or highly similar) location and fault plane solution. Therefore, if an event occurs in a location and/or with a focal mechanism solution for which there is no analog in the template catalog, it will go undetected. This may give rise to a bias in the final matched-filter catalog that would increase the uncertainty in calculating M_c and b-value. For the case of Ngatamariki and Rotokawa, although our template catalog was filtered to exclude events with high pick residuals (and therefore unreliable locations), we do not appear to have introduced any spatial bias, as shown by the similar distribution of template events relative to the raw, unfiltered catalog (compare Figure 3 to Figure S3). Also, because the template events were drawn from the exact time span over which we conducted the correlation detection, we do not anticipate having introduced a temporal bias.

The final possible bias is that the template catalog is devoid of events with a particular focal mechanism. Assuming a lack of other biases, as stated above, this would require that a particular mechanism occurred only at small magnitudes below the original amplitude-based detection threshold ($M_c \sim 0.7$). However, due to the elevated pore-pressures present at actively-produced geothermal fields, we envisage a scenario in which a variety of fracture orientations are activated. This means that the potential focal-solution space within the reservoir stress field should be relatively well sampled in the template catalog. For a particular focal mechanism solution to be missing from the template catalog, it would likely need to have been smaller than M_L 0.7 and on a fracture oriented differently from the dominant NE–SW striking pattern in the reservoirs. As such events are below M_c, they would not affect the frequency-magnitude distribution.

3. Results

3.1. Locations

The *GrowClust* relocations of the final 6479 events are shown in Figure 3. Hopp (2019) detailed the differences in locations between *GrowClust* and

Nonlinloc. From a field-wide perspective, the locations of earthquakes differ little from those presented by Sherburn et al. (2015) and Sewell et al. (2015b). The area of seismicity identified in both those studies is overlain on Figure 3 (black dot-dashed diamond) for comparison and broadly agrees with the extent of the densest seismicity in our catalog. Most events occur in the northeastern portion of the field, between the northern injection wells (RK20, RK23, RK24; Figure 1) and the northern production wells (RK13, RK14, RK25, RK29, RK30; Figure 1), with some events extending further towards the north and east. The northwest portion of the field, north of the Waikato River, as well as the southern injection zone (near wells RK21–22) exhibits little seismicity. Within the area of densest seismicity, however, our catalog more clearly reveals subclusters and structure than previous studies (Sherburn et al., 2015).

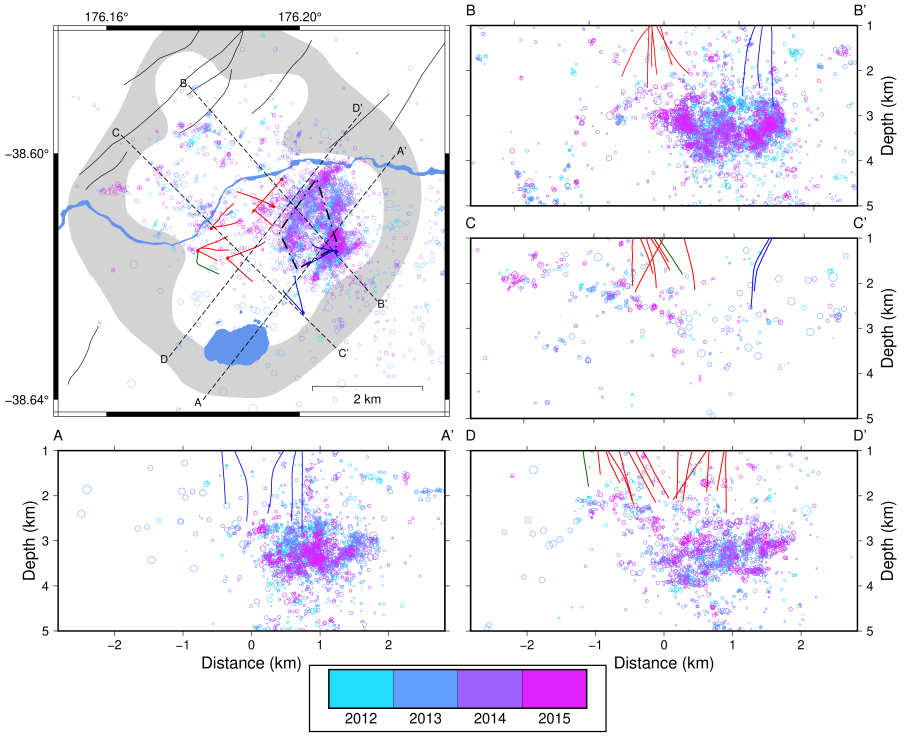

Figure 3: Seismicity at Rotokawa for the years 2012–2015 colored by date of occurrence and scaled by magnitude. All *GrowClust*-relocated events are shown. Blue events occurred earlier in the dataset and pink events occurred later. Four cross sections are plotted to show the depth distribution of seismicity and their surface projections are shown in map view. The dot-dashed diamond indicates the area of dense seismicity identified by Sherburn et al., 2015; Sewell et al., 2015b for the 2008–2012 catalog.

3.2. Magnitudes

In Figure 4a, we show the frequency-magnitude distribution for the GNS Science template events (dashed; b =1.11±0.02), matched-filter-detected events (solid, black; b =1.27±0.01) and *GrowClust*-relocated events (solid, red; b =1.10±0.02). Comparable b-values have been observed in areas of hydrothermal activity worldwide, including at the Ngatamariki geothermal field, located ∼7 km to the north (Figures 4b and S3) (e.g. Bachmann et al., 2012; Wiemer and McNutt, 1997; Dinske and Shapiro, 2012; Hopp et al., 2019). However, cases of fluid-induced b values well below 1 have also been observed (for instance $b = 0.73$ at Pohang, South Korea Ellsworth et al., 2019).

The matched-filter catalog has a larger b-value than either the template catalog or the final *GrowClust*-located catalog. We interpret this as an indication that the template catalog was not complete to the calculated M_c (0.58) and that the matched-filter detection routine augmented the lower-magnitude portions of the catalog with events that had evaded amplitude-based detection due to high noise levels. The *GrowClust*-located catalog contains fewer of these lower-magnitude events than the full matched-filter catalog and more than the template catalog. This is likely because low-amplitude waveforms are more poorly correlated with other events, a measure that *GrowClust* uses to cluster events. If an event belongs to its own cluster in the *GrowClust* algorithm, it does not get relocated, and is therefore not included in our final catalog (Trugman and Shearer, 2017).

In areas of active volcanism, as well as in both hydrocarbon and geothermal reservoir settings, b-values far exceeding 1.0 (or even 2.0) are commonly reported (e.g. Dinske and Shapiro, 2012; Shapiro et al., 2011). In general, b-values above 1.0 have been attributed to the presence of fluids, high pore-fluid pressures and geologic complexity (Wiemer, 2000; Langenbruch and Shapiro, 2014). Elevating the pore pressure allows fractures to fail that are not optimally-oriented in the local stress field. These fractures experience smaller differential stress than those which are critically stressed, and may therefore produce smaller-magnitude earthquakes when they fail (Bachmann et al., 2012). It has also been suggested that the presence of a strong thermal gradient (e.g. related to a magmatic intrusion or injection of cold water) could aid in development of small, tensional fractures (Warren and Latham, 1970), thereby increasing the population of small fractures, which can only fail in small-magnitude events. Both the elevation of pore pressure and the application of a strong thermal gradient may increase the frequency of small-magnitude seismic slip and therefore raise the b-value above typical values of ∼1.0. Figure 4b also shows the b-value at Rotokawa in comparison to the values for the two clusters of seismicity at the nearby Ngatamariki geothermal field calculated by Hopp et al. (2019).

4. Discussion

4.1. Compartmentalization

As shown in Figure 1 and discussed in Section 1.3, the Rotokawa reservoir is known to be disected into a number of compartments, at least three in the

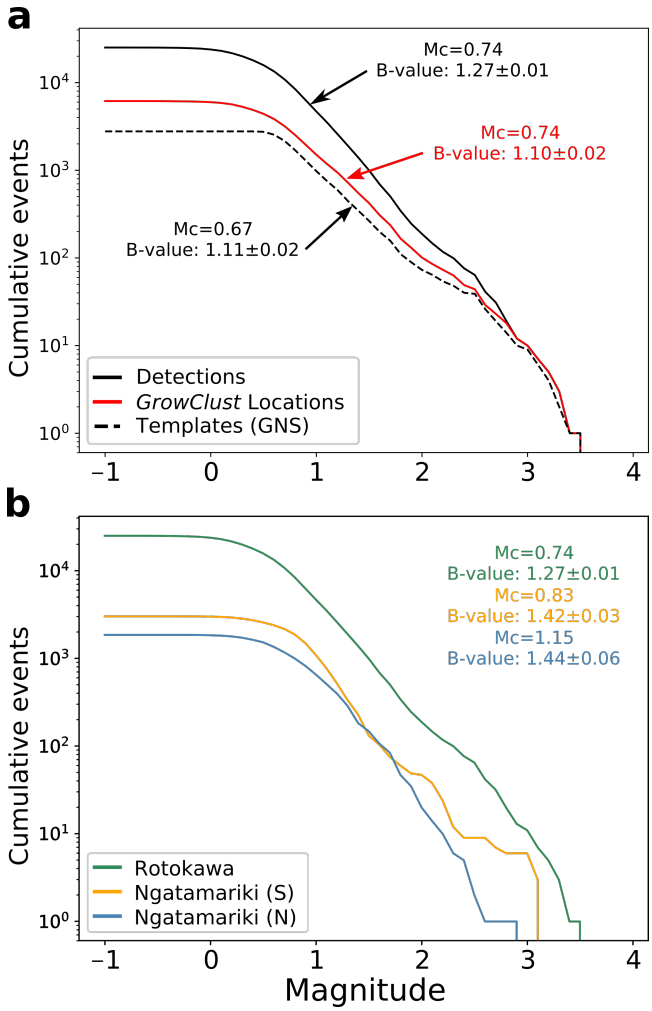

Figure 4: Top panel: Frequency-magnitude distributions for the GNS Science (dotted), matched-filter-detected (solid, black) and GrowClust-relocated (solid, red) catalogs at Rotokawa from 2012–2015. The calculated magnitude of completeness and b-value are indicated and color coded to each catalog. Bottom panel: Frequency-magnitude distributions for the full matched-filter catalog at Rotokawa compared to northern and southern Ngatamariki. The M_c and b-value for each catalog are noted in the top right, color coded to the corresponding curves. All curves represent the cumulative number of earthquakes above a given magnitude.

production field and one in the injection field. Seismicity patterns are of limited use in delineating the borders of the production field compartments because relatively few earthquakes occur in that portion of the field. However, our relocations (Figures 3 and 5) impose further constraints on the locations of the Central Field Fault (CFF) and the Injection Field Fault, and may provide

evidence for previously unidentified subcompartments within the injection field.

There are at least two NE–SW-striking sub-linear features revealed by this catalog, outlined and labeled in bold red in Figure 5. One feature lies between the injection and production fields with an arcuate shape, concave towards the southeast. This structure is likely the CFF as it sits between the injection field and the central production compartment, as previously modeled by Wallis et al. (2013). The other structure strikes NE–SW between wells RK20/24 and well RK23, and extends towards the northeast. We therefore interpret this to be the IFF, again due to the consistency of its location with known geologic and temperature offsets. The IFF was not previously imaged by microseismicity, nor has the offset between what appear to be CFF-related and IFF-related events been previously identified (Sherburn et al., 2015). There are three possible reasons for this:

1. We are able to more clearly define structures as a result of the larger number of events in our catalog;
2. The location changes may actually reflect reservoir-scale changes in permeability and fluid flow between 2012 and the end of 2015;
3. The different location algorithms used in the most recent previous study (TomoDD) (Sherburn et al., 2015) and this one (*GrowClust*) and their differing treatment of the velocity model (3D vs 1D) produced different location results

We cannot rule out the possibility of large-scale migrations in the seismically-active portion of the reservoir. For example, deepening of seismicity has been observed at The Geysers geothermal field (e.g. Martínez-Garzón et al., 2014; Jeanne et al., 2015a). However, the change in algorithm and velocity model treatment almost certainly contribute to the location discrepancy between catalogs.

A third potential structure is outlined in dotted red striking NW–SE (Figure 5). This feature is less distinct than the CFF and IFF and we are less confident about its existence. Furthermore, no major cross-strike (NW–SE) structures have been identified from offsets in well cuttings. However, along-strike variations in pressure drawdown and tracer returns do indicate that the reservoir is likely divided not only by NE–SW-striking structures, but also by NW–SE-striking structures (Sewell et al., 2015a; Quinao et al., 2013). Specifically, the contrast between the >4 MPa drawdown in the western production field (green box, Figure 1) and the 3 MPa drawdown at the northern production wells (red box, Figure 1) suggests the existence of NW–SE structures.

The following analysis is based on the hypothesis that pressure differentials between compartments may exhibit as variations in seismic characteristics. Therefore, we have divided the area of densest seismicity into three potential compartments bounded loosely by the inferred locations of the major faults and the potential NE–SW structure mentioned above (Figure 5). The light blue polygon in Figure 5 will be referred to as the western compartment and the coral and pink polygons will be referred to as the northeastern and southeastern com-

partments, respectively. These divisions are based on hypocentral locations only and constitute potential compartments that have not been identified previously.

4.2. Compartment characteristics

To begin analyzing the spatial variation in seismicity at Rotokawa, we plot the cumulative number of events, the normalized (by the total number) cumulative number of events (Figure 6a-b) and the frequency-magnitude distribution (Figure 6c) in each compartment defined in Figure 5. Panels a and b do not reveal striking differences in the rates of seismicity between compartments, with the exception of an increased rate of events in the northeast compartment (coral-colored) relative to the others at the end of 2012, which will be investigated in Section 5. However, panel c reveals a significant variation in b-value between compartments. While the western and northeastern compartments have b-values of 0.99±0.03 and 0.88±0.04, respectively, the b-value in the southeast compartment is markedly higher (1.18±0.04). Given that the southeast compartment is the closest to the main injection wells (RK20, RK23 and RK24), this may suggest that the b-value at Rotokawa is related to pore-fluid pressure, which is most elevated near injection wells. A similar, but stronger, effect was observed by Bachmann et al. (2012) at the Basel injection site in Switzerland, who found b-values exceeding 2.0 near the injection interval, albeit for wellhead pressures an order of magnitude higher (30 MPa) than used at Rotokawa (<2 MPa) (Häring et al., 2008).

As addressed in Section 2.6, the b-value for the template catalog is lower than for the *GrowClust*-relocated catalog. A similar effect is observed when the template catalog is divided into the same compartments as in Figure 6c. Thus, while the difference in b-value between template and *GrowClust*-relocated catalogs is ∼0.1–0.2, the variations in b-value between compartments remain, with the southeastern compartment exhibiting a significantly higher b-value than either the western or northeast compartments (Figure S4).

To test the significance of the compartment b-value variations, we use the approach of Utsu (1999) whereby the probability that any two sub-catalogs come from the same population is given as (Wiemer et al., 1998)

$$P \approx \exp(-dA/2 - 2) \tag{6}$$

Here, dA is the difference in the Akaike Information Criterion between the null hypothesis (i.e. both catalogs have the same b-value) and the hypothesis that their b-values are distinct. In detail,

$$dA = -2 \ln N + 2N_1 \ln N_1 + N_2 b_1/b_2 + 2N_2 \ln N_1 b_2/b_1 + N_2 - 2 \tag{7}$$

where N_1 and N_2 are the number of events in the two catalogs being compared, $N = N_1 + N_2$ and b_1 and b_2 are the b-values of the individual catalogs.

Using this method, we find that elevated b-value in the southeast compartment is significant at the 99.98% level or greater relative to those in either of the western and northeastern compartments.

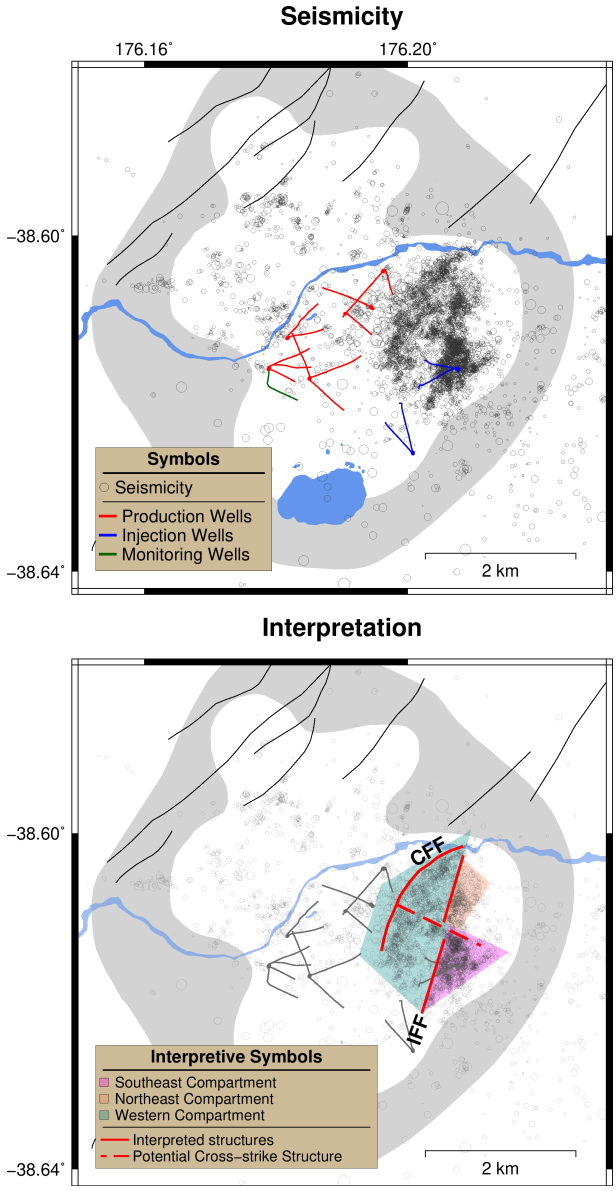

Figure 5: Seismicity at Rotokawa from 2012–2015, relocated with *GrowClust*. The top panel shows seismicity as black circles, scaled to each earthquake's magnitude (as in Figure 3). The bottom panel shows our interpretation of reservoir structure from the location of seismicity (red lines). These structures may define reservoir compartments (colored regions). The location and orientation of the Central Field Fault and Injection Field Fault (solid red) are well-constrained by seismicity. In addition, the dotted red line indicates the location of a possible cross-strike structure north of the injection wells, which may contribute to further injection-field compartmentalization.

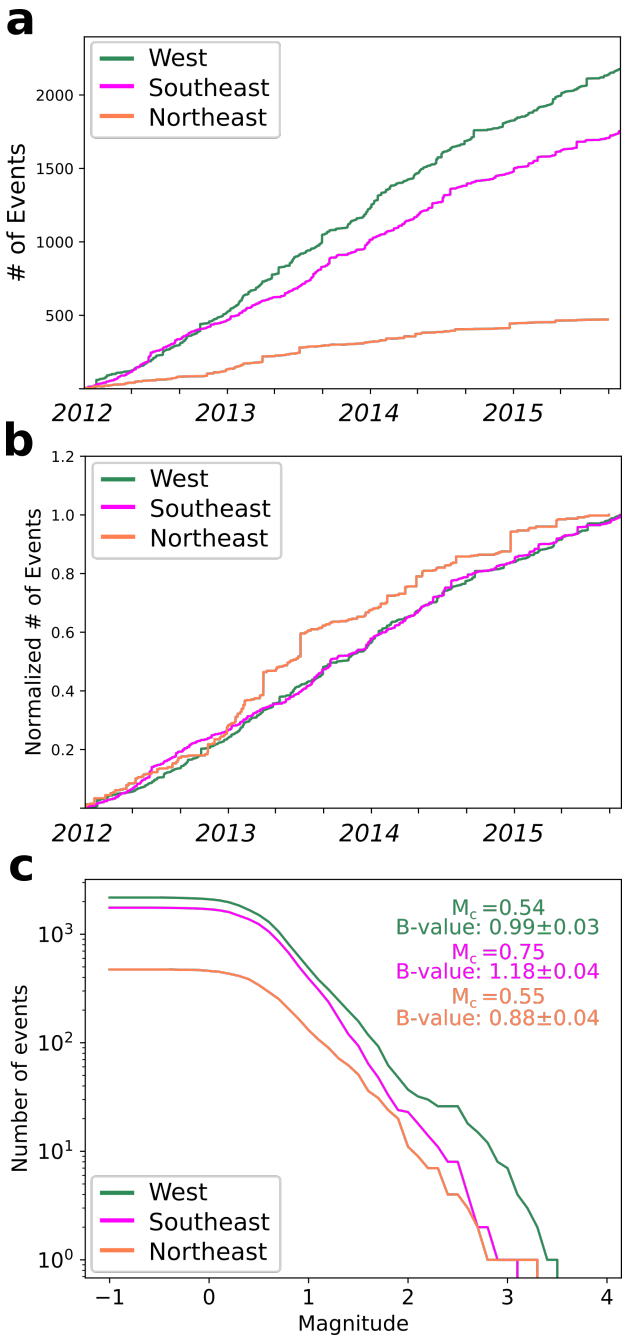

Figure 6: a) Total and b) normalized cumulative number of earthquakes in each of the three compartments defined in Figure 5. c) Frequency-magnitude distributions for each of the compartments.

5. Temporal variations in seismicity and injection parameters

As outlined in Section 1.2, the Rotokawa reservoir behaved unexpectedly during specific periods in our dataset that are of particular interest to understanding its dynamics. We address these periods below and comment on the implications for reservoir processes.

5.1. RK24 injectivity decline

Starting at the beginning of 2012, RK24, the largest injection well by percentage of injection at Rotokawa, began to suffer a decline in injectivity, meaning that it could no longer accept the same volume of fluid for a given wellhead pressure (Figure 7). This is a significant issue because economical power plant operation requires a specific enthalpy from a reservoir, and therefore a specific quantity of fluid to be extracted and reinjected. If a well cannot accept the fluid budgeted for it, that fluid must be disposed of elsewhere, which can have negative implications for resource management. In the case of RK24, the fluid was shifted to both shallow injection well RK12 and deep injection well RK23, which injects into the reservoir on the opposite side of the IFF from RK24.

As the feedzones at RK24 (and RK20) are located to the west of the IFF and may therefore be hydraulically better-connected to the western compartment (Figure 5), we expect seismicity in the western compartment to respond most readily to injection changes at these wells. Western compartment seismicity and relevant RK24 injection parameters are summarized in Figure 7. Injectivity begins to decline in the first half of 2012, after which Mercury made the decision to switch injection away from RK24. The switch can easily be seen as drop in flow rate, wellhead pressure and injectivity in July 2013 and again in July 2015.

The response of western compartment seismicity to the injectivity decline and subsequent decrease in flow at RK24 is subtle or imperceptible. In addition, the drop in WHP in July 2013 from ∼1.3 to 0.2 MPa does not produce the expected drop in the rate of seismicity. While the injectivity decline and, in particular, the subsequent pressure drop might be expected to produce significant changes in the character of seismicity, there are a number of possible reasons why the seismicity did not change. The most significant reason is that RK24 is not the only injector in this part of the field. Even if the pressure signals between RK23 and RK24 are isolated by the IFF, RK20 (on the same side of the fault as RK24) remained a significant injector throughout the dataset, injecting at a roughly constant rate of 600 t/h and a wellhead pressure of approximately 0.4 MPa. This may have provided enough pressure support in this section of the reservoir to continue to induce seismicity at close to previous rates. In addition, even as pressure had dropped at RK24, the injection rate was still ∼800 t/h. As Sherburn et al. (2015) and Sewell et al. (2015b) have assumed, Rotokawa seismicity is likely affected more by stress changes induced by reservoir cooling than reservoir pressure increases, especially near the well. The results in Figure 7 support this view as seismicity seems insensitive to pressure perturbations of as much as 1 MPa at the wellhead.

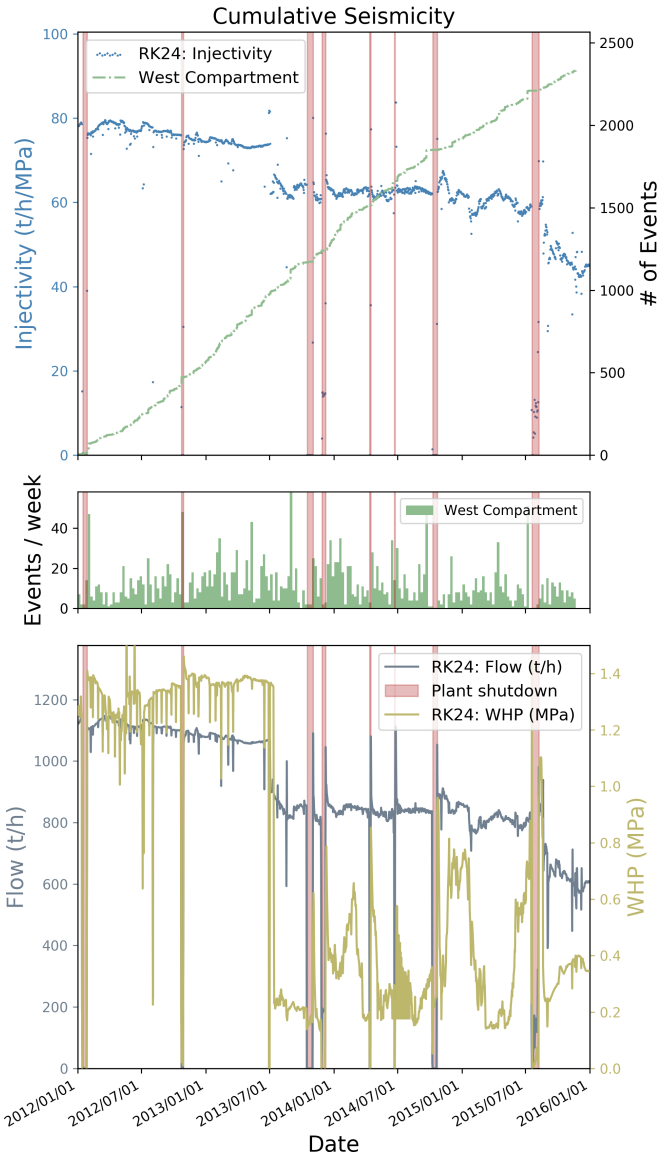

Figure 7: Seismicity in the western compartment compared to borehole parameters for well RK24 (also in the western compartment). The top panel shows the cumulative number of events (green dot-dashed) with injectivity at RK24 (blue). The middle panel shows the weekly rate of seismicity in the western compartment. The bottom panel shows both flow rate (dark gray) and wellhead pressure (yellow). Red shaded regions in all panels indicate the periods during which the power plants were shut down for maintenance, which have been recognized previously as periods of potentially heightened seismicity.

5.2. RK23 halt and restart

Most of the excess injection displaced by the RK24 injectivity decline was accounted for by shallow injection into well RK12 (in the current production field) and deep injection into RK23. Prior to this, RK23 was being used as an injector for RGEN condensate until late 2012, when it was shut for 8 months (gray bar, Figure 8) before injection of NAP brine resumed (Addison et al., 2017). In Figure 8, we plot characteristics of seismicity in the compartments that we interpret to be east of the IFF, where the pressure signal from RK23 is assumed to be the strongest. As with the western compartment, the rate of seismicity is mostly constant over time. Interestingly, the northeast compartment, furthest from RK23, experienced an increase in the rate of seismicity during the 8 months when no injection was occurring at the well, whereas the southeast compartment did not (Figure 8). This increased rate of seismicity (2–10 events/week) is still significantly lower than in the compartment near the well (5–20 events/week), but it is unclear why seismicity further from the well would respond more strongly to a pressure perturbation than seismicity nearer to the well.

5.3. Aseismic injection: RK34 drilling and RK21/RK22

One new well, RK34, was drilled at Rotokawa during our study period. Although RK34 drilling incurred full fluid losses at reservoir depths, there was no discernible response in seismicity near the well, or anywhere else in the reservoir. This behavior is distinct from the similar case of NM10 drilling in Ngatamariki the year before, which induced a significant number of events (Hopp et al., 2019). However, aseismic injection is common at Rotokawa and Ngatamariki in general (Sewell et al., 2015b). For instance, drilling and stimulation at well NM09 in Ngatamariki was largely aseismic, and injection into the southwestern injection wells, RK21/RK22, at Rotokawa has historically been aseismic (Hopp et al., 2019; Sewell et al., 2015b).

The case of RK21 and RK22 is particularly puzzling, because RK21 was used as the dominant injection well from NAP startup (>1000 t/h) until 2011, but seismicity has never been observed in this section of the field (Sewell et al., 2015b). What is more, temperature and permeability in RK21 and RK22 are highly similar to RK20/RK24. Why, then, does seismicity occur at one and not the other? Modeling at the Geysers geothermal fields has shown that density-driven, downward flow can stabilize the reservoir fracture network in regions where σ_1 is vertical (Jeanne et al., 2015a, such as at Rotokawa). Although such an effect may help explain a lack of near-well seismicity in general, it does not account for the discrepancy between wells with such similar characteristics.

6. Spatial *b*-value variations

Figures 9 and 10 reveal a complex pattern of b within the Rotokawa reservoir. The higher b-value of the southeastern compartment as a whole, shown in Figure 6c, is also discernible in Figure 9 (map view). However, b is not uniform in space

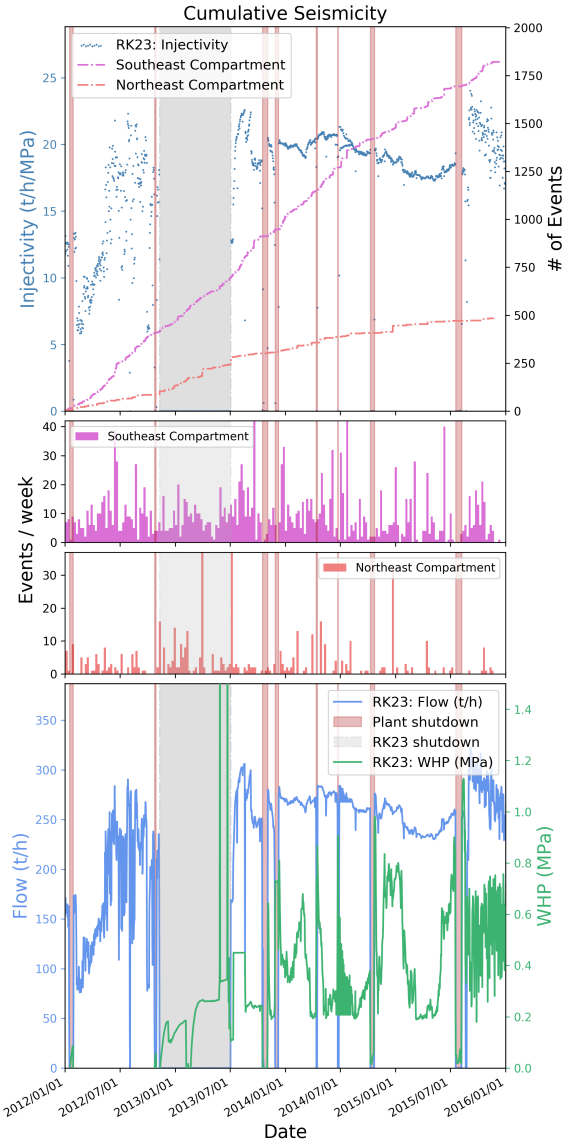

Figure 8: Seismicity in the eastern compartments compared to borehole parameters for RK23. The top panel shows the cumulative number of events (magenta and coral colored lines) with injectivity at RK23 (blue). The middle two panels show the weekly rate of seismicity in the southeastern and northeastern compartments, respectively. The bottom panel shows both flow rate (blue) and wellhead pressure (green). Red shaded regions in all panels indicate the periods during which the power plants were shut down for maintenance, which have been recognized previously as periods of potentially heightened seismicity. The period during which RK23 was shut in is shaded in gray.

throughout any of the compartments. Profiles of b-value for all compartments combined with distance from well RK23 or RK24 are shown in Figure 10c.

If we use the inferred IFF to divide the b-values into eastern and western compartments, on the basis that the pressure evolution on either side of the fault would be decoupled, the profiles take the shape of those in Figure 10a and b. In the western compartment (Figure 10b), b generally decays with distance from the well out to approximately 750 m, as predicted by the geomechanical modeling of Bachmann et al. (2012), but increases from 750 m outwards. East of the IFF, mean b-value behavior is more complicated, varying between ≈ 1.0 and 1.2 (Figure 10a).

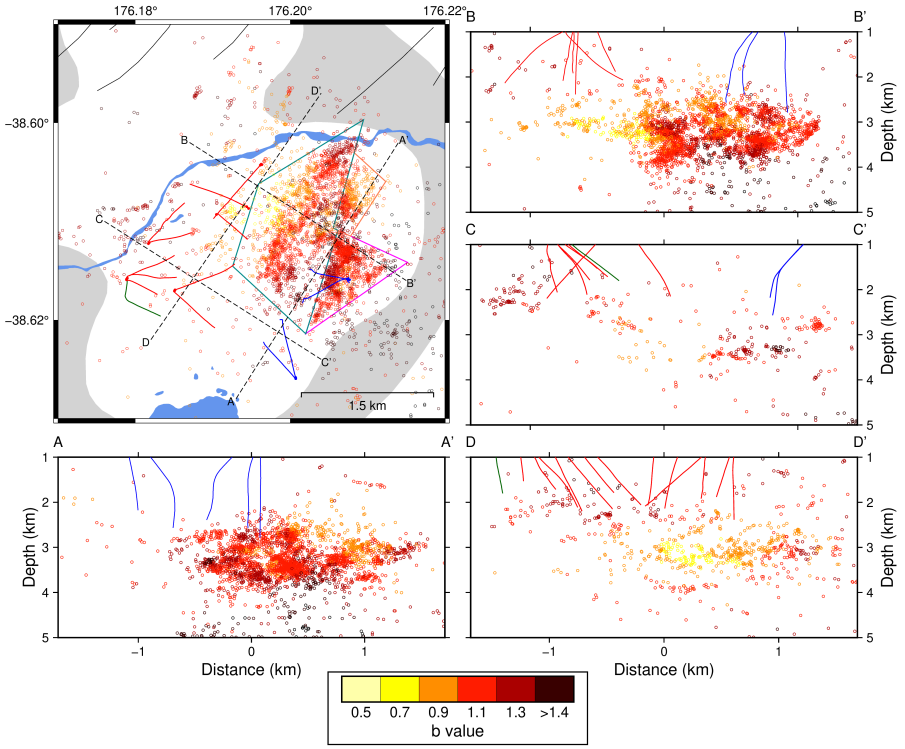

Figure 9: Spatial variation in b-value at Rotokawa. Events are colored by b-value, calculated using the nearest 300 events, provided there are at least 100 events greater than $M_c = 0.74$. The western (green polygon), northeastern (coral polygon) and southeastern (pink polygon) compartments are defined from hypocentral locations and will be relevant to the following discussion.

For all compartments combined, b-value also shows a depth dependence wherein b decreases from the surface to a minimum of $b \approx 1.0$ at 2.75 km (roughly the depth of injection; blue patches in Figure 10f) and then increases with depth until the base of seismicity at roughly 5 km. This is counterintuitive if we accept the reasoning that b-value is inversely proportional to differential

stress, which generally increases with increasing overburden at depth (Schorlemmer et al., 2005). However, Langenbruch and Shapiro (2014) suggested that the negative correlation between differential stress and b-value holds only until the boundaries of a considered rock volume are connected by critically-stressed fractures. Beyond such a point, b-value will increase with increasing differential stress as an increasing population of small fractures fail and large, critically-stressed fractures merge into a large, volume-bisecting fracture that cannot grow in size (Langenbruch and Shapiro, 2014). Given that image logs and well cuttings have revealed Rotokawa to be a highly-fractured and geologically heterogeneous reservoir (Massiot et al., 2017; McNamara et al., 2016), such an interconnected, reservoir-spanning cluster of critically-stressed fractures is plausible, perhaps explaining both the decrease in b-value to $\sim$2.5 km depth, followed by the increase in b-value with increasing depth and differential stress below. An alternative explanation for the systematic decrease in b-value at reservoir depths may be related to vertical contraction of the reservoir due to downward, density-driven flow of injectate and the resulting anisotropic cooling (see e.g. Jeanne et al., 2015a, for detailed explanation). This would produce a preferential decrease in σ_1 ($\approx \sigma_V$ at Rotokawa), thereby decreasing the differential stress in the reservoir and counteracting the effect of pore-pressure buildup.

Langenbruch and Shapiro (2014) also modeled an increase in b-value from 0.45 to 0.95 by varying the degree of complexity of the measured fractal distribution (i.e. heterogeneity) in the elastic properties of the KTB borehole host rock. Drilling at Ngatamariki has shown that intrusive bodies and dikes exist at depths <3 km in the Taupō Volcanic Zone (Chambefort et al., 2016) and geochemical evidence suggests a similar intrusive body may sit below Rotokawa (Winick et al., 2009). However, the nature of the heat source below Rotokawa is unknown (Wilson and Rowland, 2016) and it is therefore difficult to argue that geologic heterogeneity increases with depth below the base of the reservoir.

Finally, it is possible that the depths presented for our catalog are systematically too deep, due to our lack of knowledge of the S-wave velocity structure in the field. Errors reported by bootstrap resampling of the input data used by *GrowClust* indicate an average horizontal uncertainty of 200 m and an average depth uncertainty of 278 m. To test this hypothesis, we relocated the catalog using only P-picks, and also using V_P/V_S ratios of 1.86 and 2.0 (compared to $V_P/V_S = 1.72$ presented here), all of which failed to change the depth dependence of b-value in the catalog. Once work is completed on a 3-D tomographic velocity model of the Ngatamariki and Rotokawa geothermal fields (following Sewell et al., 2017), we may be better able to shed light on the depth uncertainties of seismicity at Rotokawa.

7. Conclusions

We analyze a four-year catalog of seismicity (2012–2015) for the Rotokawa geothermal field, corresponding to the four years immediately following the periods analyzed by Sherburn et al. (2015) and Sewell et al. (2015b). While seismic-

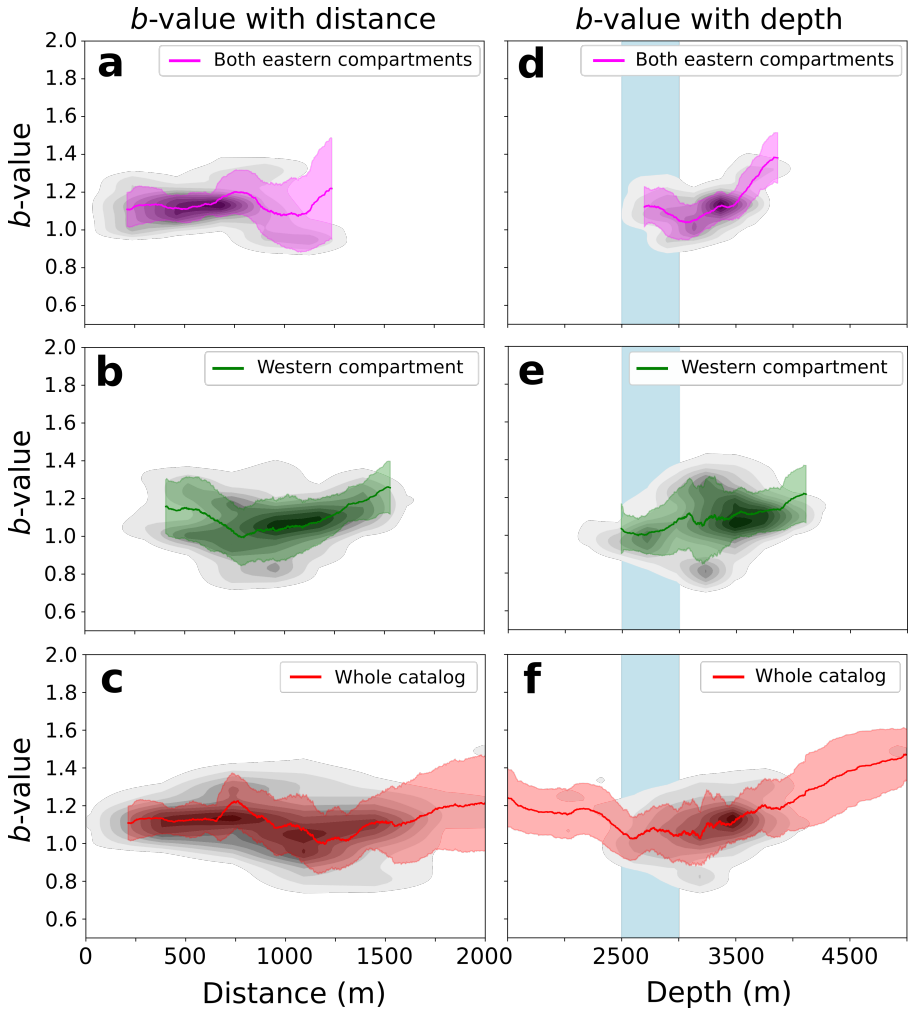

Figure 10: *b*-values with radius from the bottom of injection wells. RK23 (panels a and c) and RK24 (panel b). Panel a) shows the distance from RK23 to all events in both eastern compartments, combined. Panel b) shows the distance from well RK24 to all events in the western compartment. Panel c) shows the distance from RK23 to all events in the catalog. For all panels, the solid line shows the mean *b* in a moving window of 200 events with the filled area showing one standard deviation. The statistics are plotted starting only once the window reaches a minimum of 200 events (moving from the left). Panels d, e and f show the *b*-value distribution with depth for the catalogs in panels a, b and c with the blue patches indicating the approximate depth of injection from wells RK23 and RK24. The underlying data for all panels are plotted at a gray heatmap with darker areas showing the areas of highest density.

ity during these four years is confined to the injection field, our catalog is able to identify structures within this compartment, revealing previously unknown compartmentalization in this part of the reservoir. The locations presented are

able to further constrain the location and orientation of the Central Field Fault, and for the first time define the location of the Injection Field Fault, previously mapped only through vertical well cutting offsets and temperature gradients between wells. In addition, we have identified a new structure, cutting across the dominant NE–SW structural grain. This structure may help explain the apparent pressure 'leak' between the injection field and central production compartment identified by tracer testing (Addison et al., 2017), where previously no pressure support was identified.

Finally, we have mapped the magnitude-frequency distribution (b-value) in the reservoir. The pattern revealed is complex and fails to conform to a simplified model wherein b decays exponentially with distance from a pressure source (Bachmann et al., 2012). However, b is different between our inferred compartments. Specifically, b is higher to the east of the Injection Field Fault, suggesting that pressure may not be diffusing as readily in this section of the injection field, allowing non-critically-stressed fractures to fail more often than in other compartments. This hypothesis could be tested by observing the distribution of focal mechanism orientations east and west of the IFF, with areas of high pore-fluid pressure expected to exhibit a broader distribution of mechanisms. It is possible that b-mapping at fields elsewhere could help to identify areas of the reservoir with large pressure gradients or changes in the degree of fracturing, which might exhibit as changes in the seismic b-value. We suggest that these and other similar uses of earthquake magnitude information should be used more often as a tool for reservoir understanding and management.

8. Acknowledgments

Funding for this research and permission to publish our findings came from the Rotokawa Joint Venture (Tauhara North No. 2 Trust & Mercury NZ Limited). We thank Ian Richardson at Mercury for helpful discussions of the content of the paper and Contact Energy for providing seismic waveforms. We wish to acknowledge the contribution of New Zealand's high-performance computing facilities to the results of this research. New Zealand's national facilities are provided by the NZ eScience Infrastructure (NeSI) and funded jointly by NeSI's collaborator institutions and the Ministry of Business, Innovation & Employment's Research Infrastructure program
(https://www.nesi.org.nz). The analysis reported here made use of the ObsPy seismic processing toolbox (Team, 2019), and the matched-filter detection was conducted using the EQcorrscan package (Chamberlain et al., 2017, 2018) which can be freely downloaded and installed via *PyPI* or *Anaconda* on all major platforms. The documentation is hosted at *ReadTheDocs*. Most of the figures included in this work were made using the Matplotlib toolbox for Python (Hunter, 2007; Caswell et al., 2019).

We thank J. Ole Kaven and an anonymous reviewer for their constructive comments, which greatly improved this manuscript.

The final version of the Rotokawa earthquake catalog can be found at DOI

10.17605/OSF.IO/C2M6U along with access to the github repository that contains all of the Python scripts used in this work.

References

Addison, S., Sirad-Azwar, L., Clearwater, J., Hernandez, D., Mountain, B., Blair, A., Siratovich, P., 2017. Improving the conceptual understanding through a recent injection of 200 GBq of iodine-125 at the Rotokawa geothermal field, New Zealand, in: 42nd Workshop on Geothermal Reservoir Engineering.

Addison, S., Winick, J., Mountain, B., Siega, F., 2015. Rotokawa reservoir tracer test history, in: Proc. NZ Geothermal Workshop.

Aki, K., 1965. Maximum likelihood estimate of b in the formula log N= a-bM and its confidence limits. Bull. Earthq. Res. Inst., Tokyo Univ. 43, 237–239.

Bachmann, C.E., Wiemer, S., Goertz-Allmann, B.P., Woessner, J., 2012. Influence of pore-pressure on the event-size distribution of induced earthquakes. Geophysical Research Letters 39. doi:10.1029/2012gl051480.

Castellazzi, C., Savage, M.K., Walsh, E., Arnold, R., 2015. Shear wave automatic picking and splitting measurements at Ruapehu volcano New Zealand. Journal of Geophysical Research: Solid Earth 120, 3363–3384. doi:10.1002/2014jb011585.

Caswell, T.A., Droettboom, M., Hunter, J., Lee, A., Firing, E., Stansby, D., Klymak, J., de Andrade, E.S., Nielsen, J.H., Varoquaux, N., Hoffmann, T., Root, B., Elson, P., May, R., Dale, D., Lee, J.J., Seppnen, J.K., McDougall, D., Straw, A., Hobson, P., Gohlke, C., Yu, T.S., Ma, E., Vincent, A.F., Silvester, S., Moad, C., Katins, J., Kniazev, N., Ariza, F., Ernest, E., 2019. matplotlib/matplotlib: Rel: v3.1.1. URL: https://doi.org/10.5281/zenodo.3264781, doi:10.5281/zenodo.3264781.

Chambefort, I., Buscarlet, E., Wallis, I.C., Sewell, S., Wilmarth, M., 2016. Ngatamariki Geothermal Field New Zealand: Geology, geophysics, chemistry and conceptual model. Geothermics 59, 266–280. doi:10.1016/j.geothermics.2015.07.011.

Chamberlain, C., Hopp, C., Scott, C., Derrick, FelixHa, xiansch, Badger, T.G., Bot, S., Warren-Smith, E., 2018. eqcorrscan/EQcorrscan: EQcorrscan v. 0.3.3 release candidate 0. URL: https://doi.org/10.5281/zenodo.1894681, doi:10.5281/zenodo.1894681.

Chamberlain, C.J., Boese, C.M., Townend, J., 2017. Cross-correlation-based detection and characterisation of microseismicity adjacent to the locked late-interseismic Alpine Fault, South Westland, New Zealand. Earth and Planetary Science Letters 457, 63–72. doi:10.1016/j.epsl.2016.09.061.

Clearwater, J., Azwar, L., Barnes, M., Wallis, I., Holt, R., 2015. Changes in injection well capacity during testing and plant start-up at Ngatamariki, in: World Geothermal Congress.

Cole, B., Legmann, H., 1998. The Rotokawa Geothermal Project-A High Pressure, Sustainable and Environmentally Benign Power Plant. TRANSACTIONS-GEOTHERMAL RESOURCES COUNCIL , 509–514.

Cole, J., Lewis, K., 1981. Evolution of the Taupo-Hikurangi subduction system. Tectonophysics 72, 1–21. doi:10.1016/0040-1951(81)90084-6.

DeMets, C., Gordon, R.G., Argus, D.F., Stein, S., 1994. Effect of recent revisions to the geomagnetic reversal time scale on estimates of current plate motions. Geophysical Research Letters 21, 2191–2194. doi:10.1029/94gl02118.

Diehl, T., Deichmann, N., Kissling, E., Husen, S., 2009. Automatic S-Wave picker for local earthquake tomography. Bulletin of the Seismological Society of America 99, 1906–1920. doi:10.1785/0120080019.

Dinske, C., Shapiro, S.A., 2012. Seismotectonic state of reservoirs inferred from magnitude distributions of fluid-induced seismicity. Journal of Seismology 17, 13–25. doi:10.1007/s10950-012-9292-9.

Ellsworth, W.L., Giardini, D., Townend, J., Ge, S., Shimamoto, T., 2019. Triggering of the pohang, korea, earthquake (m w 5.5) by enhanced geothermal system stimulation. Seismological Research Letters 90, 1844–1858.

Garcia, J., Hartline, C., Walters, M., Wright, M., Rutqvist, J., Dobson, P.F., Jeanne, P., 2016. The Northwest Geysers EGS Demonstration Project California. Geothermics 63, 97–119. doi:10.1016/j.geothermics.2015.08.003.

Gutenberg, B., Richter, C.F., 1942. Earthquake magnitude, intensity, energy, and acceleration. Bulletin of the Seismological Society of America 32, 163–191.

Hanks, T.C., Kanamori, H., 1979. A moment magnitude scale. Journal of Geophysical Research 84, 2348. doi:10.1029/jb084ib05p02348.

Häring, M.O., Schanz, U., Ladner, F., Dyer, B.C., 2008. Characterisation of the basel 1 enhanced geothermal system. Geothermics 37, 469–495.

Hopp, C., 2019. Characterizing microseismicity at the Rotokawa and Ngatamariki geothermal fields. Ph.D. thesis. Victoria University of Wellington.

Hopp, C., Sewell, S., Mroczek, S., Savage, M., Townend, J., 2019. Seismic response to injection well stimulation in a high-temperature, high-permeability reservoir. Geochemistry, Geophysics, Geosystems doi:10.1029/2019GC008243.

Hunter, J.D., 2007. Matplotlib: A 2d graphics environment. Computing in Science & Engineering 9, 90–95. doi:10.1109/MCSE.2007.55.

Jeanne, P., Rutqvist, J., Dobson, P.F., Garcia, J., Walters, M., Hartline, C., Borgia, A., 2015a. Geomechanical simulation of the stress tensor rotation caused by injection of cold water in a deep geothermal reservoir. Journal of Geophysical Research: Solid Earth 120, 8422–8438. doi:10.1002/2015jb012414.

Jeanne, P., Rutqvist, J., Rinaldi, A.P., Dobson, P.F., Walters, M., Hartline, C., Garcia, J., 2015b. Seismic and aseismic deformations and impact on reservoir permeability: The case of EGS stimulation at The Geysers California, USA. Journal of Geophysical Research: Solid Earth 120, 7863–7882. doi:10.1002/2015jb012142.

Keranen, K.M., Weingarten, M., 2018. Induced seismicity. Annual Review of Earth and Planetary Sciences 46, 149–174.

Kissling, E., Ellsworth, W.L., Eberhart-Phillips, D., Kradolfer, U., 1994. Initial reference models in local earthquake tomography. Journal of Geophysical Research: Solid Earth 99, 19635–19646. doi:10.1029/93jb03138.

Krischer, L., 2015. hypoDDpy: hypoDDpy 1.0 doi:10.5281/zenodo.18907.

Kwiatek, G., Bulut, F., Bohnhoff, M., Dresen, G., 2014. High-resolution analysis of seismicity induced at berlín geothermal field, el salvador. Geothermics 52, 98–111.

Langenbruch, C., Shapiro, S., 2014. Gutenberg-richter relation originates from coulomb stress fluctuations caused by elastic rock heterogeneity. Journal of Geophysical Research: Solid Earth 119, 1220–1234.

Legmann, H., Sullivan, P., 2003. The 30 MW Rotokawa I geothermal project five years of operation, in: International Geothermal Conference, pp. 26–31.

Lomax, A., Michelini, A., Curtis, A., 2014. Earthquake Location Direct, Global-Search Methods, in: Encyclopedia of Complexity and Systems Science. Springer New York, pp. 1–33. doi:10.1007/978-3-642-27737-5_150-2.

Martínez-Garzón, P., Kwiatek, G., Sone, H., Bohnhoff, M., Dresen, G., Hartline, C., 2014. Spatiotemporal changes faulting regimes, and source parameters of induced seismicity: A case study from The Geysers geothermal field. Journal of Geophysical Research: Solid Earth 119, 8378–8396. doi:10.1002/2014jb011385.

Massiot, C., Nicol, A., McNamara, D.D., Townend, J., 2017. Evidence for tectonic lithologic, and thermal controls on fracture system geometries in an andesitic high-temperature geothermal field. Journal of Geophysical Research: Solid Earth 122, 6853–6874. doi:10.1002/2017jb014121.

Matson, G., 2019. Microseismicity during geothermal stimulation at the Ngatamariki geothermal field: New detections via a matched-filter method. Master's thesis. Victoria University of Wellington.

McNamara, D.D., Sewell, S., Buscarlet, E., Wallis, I.C., 2016. A review of the Rotokawa Geothermal Field New Zealand. Geothermics 59, 281–293. doi:10.1016/j.geothermics.2015.07.007.

Mroczek, S., Savage, M., Hopp, C., Sewell, S., 2019. Anisotropy as an indicator of reservoir changes: Example from the Rotokawa and Ngatamariki geothermal fields, New Zealand. Geophysical Journal International In review.

National Academy of Sciences, 2013. Induced Seismicity Potential in Energy Technologies. National Academies Press. doi:10.17226/13355.

Quinao, J., Sirad-Azwar, L., Clearwater, J., Hoepfinger, V., Le Brun, M., Bardsley, C., 2013. Analyses and modeling of reservoir pressure changes to interpret the Rotokawa geothermal field response to Nga Awa Purua power station operation, in: 38th Workshop on Geothermal Reservoir Engineering.

Rawlinson, Z., 2011. Microseismicity Associated with Actively Exploited Geothermal Systems: Earthquake Detection and Probabilistic Location at Rotokawa and Statistical Seismic Network Design at Kawerau. Master's thesis. Victoria University of Wellington.

Riffault, J., Dempsey, D., Karra, S., Archer, R., 2018. Microseismicity cloud can be substantially larger than the associated stimulated fracture volume: The case of the Paralana enhanced geothermal system. Journal of Geophysical Research: Solid Earth doi:10.1029/2017jb015299.

Ristau, J., Harte, D., Salichon, J., 2016. A revised local magnitude (ml) scale for new zealand earthquakes. Bulletin of the Seismological Society of America 106, 398–407.

Schoenball, M., Baujard, C., Kohl, T., Dorbath, L., 2012. The role of triggering by static stress transfer during geothermal reservoir stimulation. Journal of Geophysical Research: Solid Earth 117. doi:10.1029/2012jb009304.

Schorlemmer, D., Wiemer, S., Wyss, M., 2005. Variations in earthquake-size distribution across different stress regimes. Nature 437, 539–542. doi:10.1038/nature04094.

Segall, P., 1989. Earthquakes triggered by fluid extraction. Geology 17, 942. doi:10.1130/0091-7613(1989)017<0942:etbfe>2.3.co;2.

Sewell, S., Addison, S., Azwar, L., Barnes, M., 2015a. Rotokawa Conceptual Model Update 5 years After Commissioning of the 138 MWe NAP Plant, in: Proceedings 37th New Zealand Geothermal Workshop.

Sewell, S., Savage, M., Townend, J., Bannister, S., Hutchings, L., 2017. Preliminary investigation of seismic velocity variation at the Rotokawa and Ngatamariki geothermal field, in: Proceedings 39th New Zealand Geothermal Workshop.

Sewell, S.M., Cumming, W., Bardsley, C.J., Winick, J., Wallis, I.C., Sherburn, S., Bourguignon, S., Bannister, S., 2015b. Interpretation of Microseismicity at the Rotokawa Geothermal Field, 2008 to 2012, in: World Geothermal Congress.

Shapiro, S.A., Krüger, O.S., Dinske, C., Langenbruch, C., 2011. Magnitudes of induced earthquakes and geometric scales of fluid-stimulated rock volumes. GEOPHYSICS 76, WC55–WC63. doi:10.1190/geo2010-0349.1.

Shelly, D.R., Beroza, G.C., Ide, S., 2007. Non-volcanic tremor and low-frequency earthquake swarms. Nature 446, 305–307. doi:10.1038/nature05666.

Shelly, D.R., Ellsworth, W.L., Hill, D.P., 2016. Fluid-faulting evolution in high definition: Connecting fault structure and frequency-magnitude variations during the 2014 Long Valley Caldera California, earthquake swarm. Journal of Geophysical Research: Solid Earth 121, 1776–1795. doi:10.1002/2015jb012719.

Sherburn, S., Sewell, S., Bourguignon, S., Cumming, W., Bannister, S., Bardsley, C., Winick, J., Quinao, J., Wallis, I., 2015. Microseismicity at Rotokawa geothermal field New Zealand, 2008–2012. Geothermics 54, 23–34. doi:10.1016/j.geothermics.2014.11.001.

Shi, Y., Bolt, B.A., 1982. The standard error of the magnitude-frequency b value. Bulletin of the Seismological Society of America 72, 1677–1687.

Stein, R.S., 1999. The role of stress transfer in earthquake occurrence. Nature 402, 605.

Stephens, G., Voight, B., 1982. Hydraulic fracturing theory for conditions of thermal stress, in: International Journal of Rock Mechanics and Mining Sciences & Geomechanics Abstracts, Elsevier. pp. 279–284.

Team, T.O.D., 2019. Obspy 1.1.1. URL: https://doi.org/10.5281/zenodo.1040770, doi:10.5281/zenodo.1040770.

Trugman, D.T., Shearer, P.M., 2017. GrowClust: A Hierarchical Clustering Algorithm for Relative Earthquake Relocation with Application to the Spanish Springs and Sheldon, Nevada, Earthquake Sequences. Seismological Research Letters 88, 379–391. doi:10.1785/0220160188.

Utsu, T., 1999. Representation and analysis of the earthquake size distribution: a historical review and some new approaches, in: Seismicity Patterns, their Statistical Significance and Physical Meaning. Springer, pp. 509–535.

Villamor, P., Berryman, K.R., Nairn, I.A., Wilson, K., Litchfield, N., Ries, W., 2011. Associations between volcanic eruptions from Okataina volcanic center and surface rupture of nearby active faults Taupo rift, New Zealand: Insights into the nature of volcano-tectonic interactions. Geological Society of America Bulletin 123, 1383–1405. doi:10.1130/b30184.1.

Wallace, L.M., 2004. Subduction zone coupling and tectonic block rotations in the North Island New Zealand. Journal of Geophysical Research 109. doi:10.1029/2004jb003241.

Wallis, I., Bardsley, C., Powell, T., Rowland, J., O'Brien, J., 2013. A structural model for the Rotokawa Geothermal Field, New Zealand, in: Proceedings 35th New Zealand Geothermal Workshop.

Warren, N.W., Latham, G.V., 1970. An experimental study of thermally induced microfracturing and its relation to volcanic seismicity. Journal of Geophysical Research 75, 4455–4464. doi:10.1029/jb075i023p04455.

Weber, B., Becker, J., Hanka, W., Heinloo, A., Hoffmann, M., Kraft, T., Pahlke, D., Reinhardt, J., Thoms, H., 2007. SeisComP3—Automatic and interactive real time data processing, in: Geophysical Research Abstracts.

Wiemer, S., 2000. Minimum magnitude of completeness in earthquake catalogs: Examples from Alaska the western United States, and Japan. Bulletin of the Seismological Society of America 90, 859–869. doi:10.1785/0119990114.

Wiemer, S., McNutt, S.R., 1997. Variations in the frequency-magnitude distribution with depth in two volcanic areas: Mount St. Helens Washington, and Mt. Spurr, Alaska. Geophysical Research Letters 24, 189–192. doi:10.1029/96gl03779.

Wiemer, S., McNutt, S.R., Wyss, M., 1998. Temporal and three-dimensional spatial analyses of the frequency-magnitude distribution near Long Valley Caldera California. Geophysical Journal International 134, 409–421. doi:10.1046/j.1365-246x.1998.00561.x.

Wilson, C., Houghton, B., McWilliams, M., Lanphere, M., Weaver, S., Briggs, R., 1995. Volcanic and structural evolution of Taupo Volcanic Zone New Zealand: A review. Journal of Volcanology and Geothermal Research 68, 1–28. doi:10.1016/0377-0273(95)00006-g.

Wilson, C.J., Rowland, J.V., 2016. The volcanic magmatic and tectonic setting of the Taupo Volcanic Zone, New Zealand, reviewed from a geothermal perspective. Geothermics 59, 168–187. doi:10.1016/j.geothermics.2015.06.013.

Winick, J., Powell, T., Mroczek, E., 2009. The natural-state geochemistry of the Rotokawa reservoir, in: Proceedings 31st New Zealand Geothermal Workshop.